applied optics

Resolution-enhanced imaging through scattering media by high-order correlation

Yuehan Liu,[1] Lei Chen,[2] Wei Liu,[2] Xiaogan Liang,[3] and Wenjie Wan[1,2,*]

[1]The State Key Laboratory of Advanced Optical Communication Systems and Networks, The University of Michigan-Shanghai Jiao Tong University Joint Institute, Shanghai Jiao Tong University, Shanghai 200240, China
[2]MOE Key Laboratory for Laser Plasmas and Collaborative Innovation Center of IFSA, Department of Physics and Astronomy, Shanghai Jiao Tong University, Shanghai 200240, China
[3]Department of Mechanical Engineering, University of Michigan, Ann Arbor, Michigan 48109, USA
*Corresponding author: wenjie.wan@sjtu.edu.cn

Received 29 November 2018; revised 17 February 2019; accepted 17 February 2019; posted 19 February 2019 (Doc. ID 351995); published 18 March 2019

Super-resolution optical imaging is a rapidly emerging technology enabling many applications. Recently, correlation imaging has shown its capability in imaging beyond the diffraction limit, relying on quantum and statistical properties of light. High-order correlation imaging can further enhance resolution, however, at the expense of complicated algorithms. Here, we experimentally demonstrate a resolution-enhanced method of imaging through scattering media by exploiting high-order correlation of fluorescence light. Based on this method, individual fluorophores' temporal fluctuations are recorded and computed for their distinguished high-order correlations that enable super-resolution. Special designed time sequences are chosen to reduce computation time and memory. Such high-order correlation imaging exhibits reliable performance through scattering media with significant resolution enhancement and background noise reduction. This efficient imaging method paves the way for new biomedical applications.

https://doi.org/10.1364/AO.58.002350

1. INTRODUCTION

Super-resolution imaging is a classical problem to improve the spatial resolution of optical microscopy limited by Abbe's diffraction limit of light [1], gaining several major breakthroughs in recent years. Among them, super-resolution fluorescence microscopy plays an important role in biomedical applications at the cellular or even subcellular levels [2]. Some techniques rely on patterned illumination, such as stimulated emission depletion microscopy [3] and structured illumination microscopy [4], which employ the nonlinearity of fluorescent phosphors to achieve resolution enhancement. Meanwhile, other techniques like photo-activation localization microscopy [5] and stochastic optical reconstruction microscopy [6] are based on stochastic blinking properties of fluorophores to obtain single-molecule localization with improved imaging resolution. Another scheme to beat the diffraction limit is exploring the quantum and statistical properties of light. For example, ghost imaging exploits nonlocal multi-photon interference based on the point-to-point second-order correlation between the object plane and the image plane to enable nonlocal imaging, first demonstrated with entangled photon pairs [7], and later with chaotic thermal light source [8]. Such a nonlocal imaging scheme allows remotely observing quantum interference patterns with subwavelength distribution tighter than classically allowed [9]. Furthermore, high-order ghost imaging has been put forward with potential to further improve resolution and visibility [10]. In addition, second-order correlation has been applied to image through scattering media [11,12], greatly improving image quality and resolutions.

In the meantime, correlation imaging has advanced another major step by a method called super-resolution optical fluctuation imaging (SOFI) [13], which relies on the statistical analysis of temporal fluorescence fluctuations. By computing the high-order correlations of each pixel's signal temporal trace, a higher-resolution image can be obtained directly. Unique SOFI features include compatibility with all microscopic platforms, and robustness to produce three-dimensional background-free images. Later, SOFI with speckle patterns illumination (S-SOFI) comes up with the idea of inducing controllable illumination-induced optical fluctuations [14] to extend the selectivity of blinking fluorescence fluctuations required by SOFI [15]; anti-bunching correlation can also be utilized for the imaging purpose based on statistical properties of quantum dots [16]. Another barrier to pursuing higher resolution is the huge computation time and memory space required when generating high-order images. Modified techniques, such as like cross-cumulants SOFI (XC-SOFI) [17] and Fourier-SOFI (f-SOFI) [18], can reach high resolution with rather low orders by taking the spatial correlation into consideration.

In this paper, we theoretically and experimentally demonstrate a reliable, efficient method: resolution-enhanced, high-order fluorescence correlation imaging (HG). By extracting temporal fluctuations of fluorophores and exploiting their high-order correlations, this method is capable of analyzing the statistical properties of individual emitters and distinguishing all of them from noise. We also explore the time sequence of high-order correlation functions and put forward an effective strategy to simplify computation. By choosing special time sequences, the improved algorithm largely reduces computation time and memory, with highly enhanced resolution. Furthermore, we prove HG imaging applicable to imaging through scattering media. High-order images can be easily retrieved where emitters hidden in highly scattering media are better resolved with significant background reduction and resolution enhancement.

2. CONVENTIONAL CORRELATION IMAGING

Classical optical imaging cannot resolve objects beyond the optical diffraction limit. The point spread function (PSF) describes the response of an imaging system to a point object, and its width reveals the resolving ability. In microscopy, the PSF is fully determined by the specifications of a microscope and can be approximated by a three-dimensional Gaussian distribution: $U(\mathbf{r}) = \exp(-\frac{x^2+y^2}{2\omega^2} - \frac{z^2}{2\omega_z^2})$. Traditionally, the image of any object is regarded as a convolution of the true object and the PSF. To enhance the resolution, the width of the PSF must shrink. One approach to achieving this is utilizing the temporal properties of the fluctuant object [13]: instead of taking a single shot image, a movie of hundreds or even thousands of images needs to be recorded for computing temporal correlations.

Here, consider a stationary sample labeled with N fluorescing emitters $\mathbf{r}_k$, and each of them has a time-dependent brightness $\varepsilon_k \cdot s_k(t)$. The image $F(\mathbf{r}, t)$ recorded at position $\mathbf{r}$ and time t can be given by the convolution $\sum_{k=1}^{N} U(\mathbf{r} - \mathbf{r}_k) \cdot \varepsilon_k \cdot s_k(t)$. The fluctuations of the sample can be written as zero-mean fluctuations:

$$\delta F(\mathbf{r}, t) = F(\mathbf{r}, t) - \langle F(\mathbf{r}, t)\rangle_t = \sum_k U(\mathbf{r} - \mathbf{r}_k) \cdot \varepsilon_k \cdot \delta s_k(t), \tag{1}$$

where $\langle \ldots \rangle_t$ denotes time averaging. Under the assumption that the blinking of all emitters is statistically independent from each other, the cross-correlation terms of different emitters ($k_1 \neq k_2$) vanish, with only the auto-correlation term left [13]. The second-order correlation function is then given by

$$\begin{aligned} G_2(\mathbf{r},\tau) &= \langle \delta F(\mathbf{r},t) \cdot \delta F(\mathbf{r}, t+\tau)\rangle_t \\ &= \sum_{k_1,k_2} U(\mathbf{r}-\mathbf{r}_{k_1}) \cdot U(\mathbf{r}-\mathbf{r}_{k_2}) \cdot \varepsilon_{k_1} \cdot \varepsilon_{k_2} \cdot \langle \delta s_{k_1}(t) \delta s_{k_2}(t+\tau)\rangle \\ &= \sum_k U^2(\mathbf{r}-\mathbf{r}_k) \cdot \varepsilon_k^2 \cdot \langle \delta s_k(t) \delta s_k(t+\tau)\rangle. \end{aligned} \tag{2}$$

In conventional correlation imaging, the value of $G_2(\mathbf{r}, \tau)$ for a certain time lag τ is used for generating correlation images, e.g., in ghost imaging. As shown in Eq. (2), $G_2(\mathbf{r}, \tau)$ appears as a sum of the squared PSF, which can be seen as the "new PSF" of the system. The width of this "new PSF" is reduced by a factor of $\sqrt{2}$ along all three dimensions, directly increasing resolution by $\sqrt{2}$.

For higher orders, $G_n(\mathbf{r}, \tau_1, \ldots, \tau_{n-1})$ can be obtained similarly by multiplying fluctuations for $(n-1)$ time lags:

$$\begin{aligned} G_n(\mathbf{r},\tau_1,\ldots,\tau_{n-1}) &= \langle \delta F(\mathbf{r},t) \cdot \delta F(\mathbf{r}, t+\tau_1) \cdots \delta F(\mathbf{r}, t+\tau_{n-1})\rangle_t \\ &= \sum_{k_1,\ldots,k_n} U(\mathbf{r}-\mathbf{r}_{k_1}) \cdots U(\mathbf{r}-\mathbf{r}_{k_n}) \cdot \varepsilon_{k_1} \cdots \varepsilon_{k_n} \\ &\quad \cdot \langle \delta s_{k_1}(t) \cdots \delta s_{k_n}(t+\tau_{n-1})\rangle. \end{aligned} \tag{3}$$

The expansion of Eq. (3) contains both an auto-correlation term and a large number of cross-correlation terms, which improve the resolution to a different extent. Note that the physical meaning of G_n is the correlation of n photons in one pixel: in the case of all n photons originating from the same emitter, i.e., $k_1 = k_2 = \cdots = k_n$, the cross-correlation terms totally vanish. As a result, G_n shrinks to a simple form: $U^n(\mathbf{r} - \mathbf{r}_k) \cdot \varepsilon_k^n \cdot \langle \delta s_k(t) \delta s_k(t+\tau_1) \cdots \delta s_k(t+\tau_{n-1})\rangle$, where U^n serves as a "new PSF," and its width is reduced by a factor of $\sqrt{n}$.

In order to verify the concept of conventional correlation imaging, we experimentally generate correlation images of different orders of a blinking quantum dot (QD). Figure 1(a) shows the 2nd-, 4th-, 9th-, 16th-, and 25th-order correlation images of one single QD. The dotted line in Fig. 1(a) denotes the cross section through the PSF of the emitter. This intensity cross section is fitted with a Gaussian model for all calculated orders, as plotted in Fig. 1(b). It is clear that as the correlation order goes up, the width of the PSF shrinks remarkably. Gaussian fit for the order of 25 yields a fourfold resolution enhancement, but less than the theoretical value of $\sqrt{n}$. This may be caused by the large distortion and asymmetry of the image shown in Fig. 1(a), which makes Gaussian fit less appropriate to provide desirable outcome.

In a more general setting, photons might come from more than one emitter with different brightness and blinking behavior. According to Eq. (3), unequal brightness distorts the contrast of final images, which results in the masking of dim emitters that are in close proximity to brighter ones, especially in high-order images. Because the higher the order, the larger brightness differences among pixels will grow. To remove this unwanted effect, the amplified brightness needs to be corrected by linearization, using deconvolution [14] or other similar techniques [19]. On the other hand, correlation images also depend on the behavior of each emitter. A nonfluctuating emitter does not yield any correlation, while a blinking emitter yields a nonzero value and shows up in the resulting image. Actually, correlation imaging is not limited to fluorescence fluctuations. It can be applied to imaging any fluctuating objects.

In addition, it needs to point out that the nth-order correlation function cannot guarantee a $\sqrt{n}$-fold resolution enhancement, because the expansion of $G_n(\mathbf{r}, \tau_1, \ldots, \tau_{n-1})$ contains many cross terms which lead to lower-order contributions. For example, it is possible that half of the photons come from one emitter and the other half come from a different emitter. This case would yield cross terms that consist of the nth/2-power of the PSF, concealing the nth-power PSF contribution. To ensure a $\sqrt{n}$-fold enhancement, SOFI transforms $G_n(\mathbf{r}, \tau_1, \ldots, \tau_{n-1})$ into nth-order cumulant function

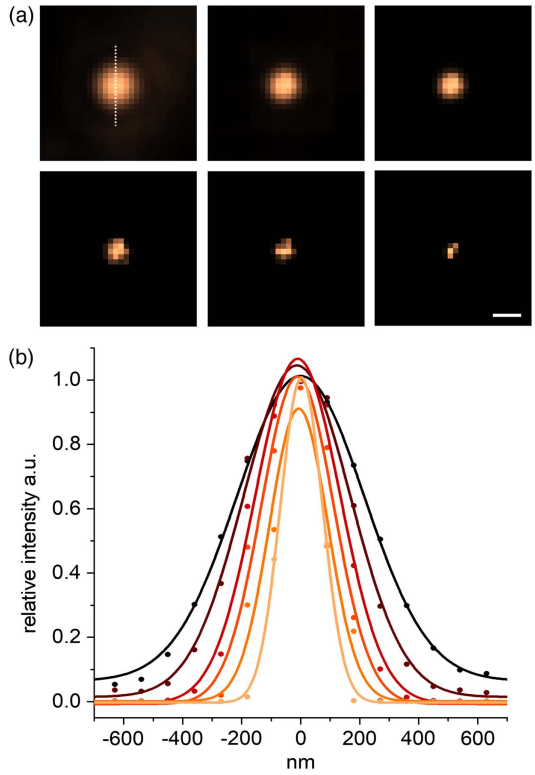

Fig. 1. Conventional high-order correlation images and enhancement of resolution. The CdSe/ZnS quantum dots (QDs) are deposited on a thin microscope slide as the observed sample. Data are recorded in series of 1000 frames (100 ms per frame). (a) Experimental results of a single QD. From upper left to lower right: mean image (mean intensity of all movie frames) and the 2nd-, 4th-, 9th-, 16th-, and 25th-order correlation images. (b) Gaussian fits of the cross section displayed in (a). Dots indicate raw data and lines show the fits. From black to orange: mean intensity and the normalized correlation intensities with increasing orders 2–25, whose full width at half-maximum (FWHM) values are 567 nm, 425 nm, 337 nm, 288 nm, 214 nm, and 141 nm, respectively. Scale bar: 500 nm.

$C_n(\mathbf{r}, \tau_1, \ldots, \tau_{n-1})$, which eliminates all cross terms [13]. But the recursive algorithm of $C_n(\mathbf{r}, \tau_1, \ldots, \tau_{n-1})$ is quite sophisticated and computation demanding [20]. In fact, although $C_n(\mathbf{r}, \tau_1, \ldots, \tau_{n-1})$ exhibits better performance, recent studies have proved that $G_n(\mathbf{r}, \tau_1, \ldots, \tau_{n-1})$ is also capable of breaking the optical diffraction limit [16,21]. For a sparse sample where individual emitters are dispersedly separated out rather than clustered together, we may expect G_n to exhibit similar performances as C_n with less computation.

3. HG IMAGING

We have previously acquired conventional correlation images with a subdiffraction limit resolution for a single emitter. When imaging several emitters simultaneously, some nonnegligible deficiencies pop up, for example, the brightness of some emitters tends to be even darker than the background. In addition, the complex computation for the high-order correlations causes great trouble. Here we demonstrate a new, superior approach—resolution-enhanced, HG imaging—to solve these issues.

In this section, all experiments are carried out using CdSe/ZnS QDs as our samples, whose blinking behavior obeys a power-law fluorescence "on"/"off" distribution [22]. The images are taken on a homebuilt inverted fluorescence microscope (Olympus objective: 100×, NA 0.95, air). A 532 nm CW laser is used as the light source. The fluctuant fluorescence of QDs is measured by an electron-multiplying CCD (EMCCD) camera (Andor iXon3). Excitation (532 nm) and emission light (630 nm) are filtered using a dichroic mirror and two long-pass filters. Magnification is adjusted to around 90 nm per pixel.

A. Blinking Analysis: Distinguish Fluctuating Emitters from Background

First, we start with the blinking behavior of CdSe/ZnS QDs. Relevant studies have found that some QDs of this type can convert frequently between "on"/"off" states, while others may stay in one state for a relatively long time [22]. In our experiment, we observe and record several QDs. Figure 2(a) plots the intensity trajectories of two individual QDs, which exhibit distinct fluctuations. According to the correlation imaging theory, the correlation brightness, i.e., the G_n value of each pixel, is not only determined by the intensity, but more importantly, by the blinking behavior of emitters. So the brightness of different emitters in the correlation images can be quite different.

To study the effect of nonuniform blinking, we calculate the second-order correlation images with different time lag values: $\tau = 0$, 100, 200, 300, 400, and display the results in Fig. 2(b). Independently in each subgraph, the second-order correlations of all pixels are linearly converted into the intensity image, by

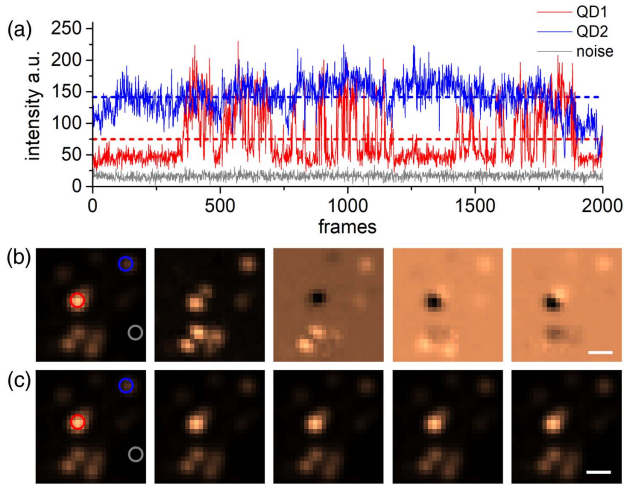

Fig. 2. Comparison between conventional and modified correlation imaging. Data are recorded in series of 2000 frames (100 ms per frame). (a) Time series of three intensity fluctuations from the raw dataset. QD1, QD2, and noise correspond to three individual pixels marked in (b) and (c) with red, blue, and gray circles, respectively. Solid lines depict real intensity trajectories and dashed lines represent the average intensities. (b) Conventional second-order correlation images with different time lags and independent brightness scales. From left to right: the time lag values are set to be 0, 100, 200, 300, and 400. In each image, the minimum $G_2(\mathbf{r}, \tau)$ value is set to 0 (black) and the maximum $G_2(\mathbf{r}, \tau)$ value is set to 1 (full brightness). (c) Results of modified second-order correlation imaging with time lags 0–400. Scale bar: 500 nm.

setting the minimum $G_2(\mathbf{r},\tau)$ value to 0 (black) and the maximum $G_2(\mathbf{r},\tau)$ value to 1 (full brightness). From the results, we discover some unusual phenomena: for a relatively long time lag in Fig. 2(b), e.g., $\tau \geq 200$, some QDs become even darker than the background, making the images unclear and ambiguous. To investigate its cause, we extract the time traces of three typical pixels representing a dark QD1, a bright QD2, and the background in Fig. 2(a). Recall that $G_2(\mathbf{r},\tau)$ describes the temporal correlation between two fluctuations with a time lag τ, which can be written as the average of a product of two differences: $\langle \delta F(\mathbf{r},t)\cdot\delta F(\mathbf{r},t+\tau)\rangle_t = \langle (F(\mathbf{r},t) - \langle F(\mathbf{r},t)\rangle_t)\cdot (F(\mathbf{r},t+\tau) - \langle F(\mathbf{r},t+\tau)\rangle_t)\rangle_t$. For a short time lag, such as $\tau = 100$, both QD1 and QD2 fluctuate more violently than the background noise, resulting in larger δF for QDs and smaller ones for the noise. So $G_2(\mathbf{r},\tau)$ of QDs are larger than that of the noise, corresponding to bright signals and dark background in the correlation images shown in Fig. 2(b). For a relatively long time lag, e.g., $\tau = 200$, 300, or 400, specific long-term blinking behavior tends to greatly influence imaging. According to Fig. 2(a), QD1 exhibits significant blinking over a long period of time. It is clear that some certain portions of its time trace are below the long-term average intensity value $\langle F(\mathbf{r},t)\rangle_t$ (the red dashed line), yielding negative δF, while other portions above the average value yield positive δF. As a result, for some large τ values, $\delta F(r,t)$ and $\delta F(r,t+\tau)$ tend to have opposite signs, leading to negative $G_2(\mathbf{r},\tau)$. However, QD2 fluctuates less markedly around the average intensity value over the total period, with a major part of the time trace slightly above the blue dashed line. That means both $\delta F(r,t)$ and $\delta F(r,t+\tau)$ are more likely to be positive even for larger τ, leading to positive $G_2(\mathbf{r},\tau)$. In the case of the uncorrelated noise, it displays random and very slight fluctuations right around its average, i.e., $F(\mathbf{r},t) \approx \langle F(\mathbf{r},t)\rangle_t$ during the whole period. So $G_2(\mathbf{r},\tau)$ of the background noise can be a time-independent and near-zero value. Therefore, QD1 appears to be a dark spot compared to the background, while QD2 exhibits as a bright one in Fig. 2(b).

To address this problem, we revise the conventional G_n formula by using the absolute values of all fluctuation terms. As a result, these terms are no longer canceled with each other and the final outcome is always positive. In such a way, information of the fluctuations can be retained completely. The modified second-order correlation imaging function HG_2 is written as

$$\begin{aligned}\mathrm{HG}_2(\mathbf{r},\tau) &= \langle |\delta F(\mathbf{r},t)\cdot\delta F(\mathbf{r},t+\tau)|\rangle_t \\ &= \sum_k U^2(\mathbf{r}-\mathbf{r}_k)\cdot\varepsilon_k^2\cdot\langle|\delta s_k(t)s_k(t+\tau)|\rangle_t. \end{aligned} \quad (4)$$

The results of $\mathrm{HG}_2(\mathbf{r},\tau)$ with time lags from 0 to 400 are shown in Fig. 2(c). Using absolute values, desirable images are obtained with good quality even for longer time lags. More importantly, the correlation intensities of all emitters are higher than the background noise no matter how different their blinking rates are, which relaxes the requirement for fluorophores. This algorithm can also be generalized to higher orders as $\mathrm{HG}_n(\mathbf{r},\tau_1,\ldots,\tau_{n-1}) = \langle|\delta F(\mathbf{r},t)\cdot\delta F(r,t+\tau_1)\cdots\delta F(r,t+\tau_{n-1})|\rangle_t$. Given the complexity of computation, time lags are usually set as one. In this case, we have experimentally validated resolution-enhanced high-order imaging, where all blinking emitters can be distinguished from the background.

B. Time Sequence: Reduce the Dimensions of High-Order Correlations

Higher-order correlation is capable of achieving higher resolution, but intractable computation largely diminishes its utility. Although there is no fundamental difficulty in calculating the multi-dimensional function $\mathrm{HG}_n(\mathbf{r},\tau_1,\ldots\tau_{n-1})$, the computation time and memory consumption grow quadratically as n^2 [13]. In order to overcome this limitation, we propose a fast, efficient way to simplify the algorithm by reducing the dimensions of high-order correlations.

We notice that in the field of thermal light ghost imaging, correlation of chaotic thermal light is used to analyze the statistical correlation of intensity fluctuations: Shih *et al.* presented a unified theory of the *n*th-order correlation of thermal light and experimentally measured the third-order spatial correlation function [23]. Later, other researchers found that the "directionality" of spatial third-order correlation function can influence both the resolution and the contrast of ghost imaging [10,24]. Inspired by these studies, we explore the corresponding "time sequence" of temporal high-order correlation functions.

To measure the third-order spatial correlation function, three point detectors need to be placed at different positions. The mathematical expression of normalized third-order correlation has been derived with a form depending on the distances between these detectors [23]. While the third-order temporal correlation function can be measured with one detector recording a movie, and the normalized function can be defined as a two-dimensional function of the time lags between different movie frames, i.e., $\tau_{01} \equiv \tau_1 - \tau_0$ and $\tau_{02} \equiv \tau_2 - \tau_0$:

$$\begin{aligned}\mathrm{HG}_3(\tau_{01},\tau_{02}) &= \langle|\delta F(\mathbf{r},t+\tau_0)\cdot\delta F(\mathbf{r},t+\tau_1)\cdot\delta F(\mathbf{r},t+\tau_2)|\rangle_t \\ &= \langle|\delta F(\mathbf{r},t)\cdot\delta F(\mathbf{r},t+\tau_{01})\cdot\delta F(\mathbf{r},t+\tau_{02})|\rangle_t. \end{aligned} \quad (5)$$

The top view of the histogram of theoretical $\mathrm{HG}_3(\tau_{01},\tau_{02})$ is displayed in Fig. 3(a). To analyze its property, we compare the widths of $\mathrm{HG}_3(\tau_{01},\tau_{02})$ with different time series.

In the case of $\tau_{01} = \tau_{02}$, corresponding to the top-right to bottom-left diagonal in Fig. 3(a), HG_3 is simplified as

$$\mathrm{HG}_3(\tau_{01},\tau_{01}) = 2 + 4\ \mathrm{sinc}^2(\beta\cdot\tau_{01}), \quad (6)$$

where β is a numerical coefficient.

While in another case of $\tau_{01} + \tau_{02} = 0$, corresponding to the other diagonal from top-left to bottom-right, we have

$$\begin{aligned}\mathrm{HG}_3(\tau_{01},-\tau_{01}) &= 1 + \mathrm{sinc}^2(2\beta\cdot\tau_{01}) + 2\ \mathrm{sinc}^2(\beta\cdot\tau_{01}) \\ &\quad + 2\ \mathrm{sinc}(2\beta\cdot\tau_{01})\ \mathrm{sinc}^2(\beta\cdot\tau_{01}). \end{aligned} \quad (7)$$

Results show that Eq. (7) has a narrower FWHM [only around 70% of the FWHM of Eq. (6)] and lower constant background [1 for Eq. (7) and 2 for Eq. (6)]. This feature reflects the "time sequence" of temporal third-order correlation function. As previously mentioned, the high-order correlation function appears as a sum of the high-order power of the PSF, which can be regarded as a "new PSF" of the imaging system; in other words, the width of HG_n determines the imaging quality. Therefore, $\mathrm{HG}_3(\tau_{01},-\tau_{01})$ definitely leads to higher resolution and lower

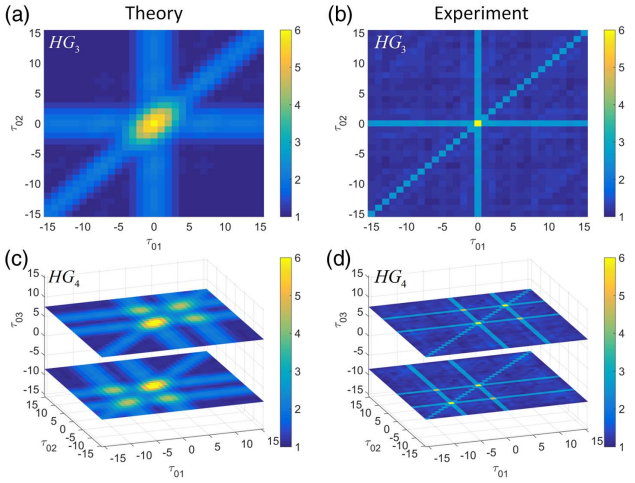

Fig. 3. Time sequence of high-order temporal correlation functions. Theoretical results are calculated based on normalized temporal functions. Experimental results are obtained based on the time series of a certain pixel with fluctuating brightness. Data are recorded in series of 1000 frames of blinking QDs (100 ms per frame). The third-order correlation is plotted as a function of $\tau_{01} \equiv \tau_1 - \tau_0$ and $\tau_{02} \equiv \tau_2 - \tau_0$: (a) theoretical HG_3, (b) experimental HG_3. The fourth-order correlation is plotted as a function of τ_{01}, τ_{02}, and $\tau_{03} \equiv \tau_3 - \tau_0$: (c) theoretical HG_4, (d) experimental HG_4. Each slice represents the data for a fixed τ_3.

background; meanwhile, it is reduced to a one-dimensional function which only relies on τ_{01}.

Experimentally, we measure the temporal third-order correlation function $HG_3(\tau_{01}, \tau_{02})$ and plot it in Fig. 3(b). The minimum units of τ_{01} and τ_{02} are both 100 ms, which are determined by the time interval between two adjacent frames. As a result, Fig. 3(b) tends to be not as elaborate as Fig. 3(a). Even though it clearly shows the time sequence of HG_3. For more-refined results, faster frame rates, i.e., shorter time intervals, are required.

In order to investigate the time sequence of higher order, we compute the theoretical normalized fourth-order correlation function $HG_4(\tau_{01}, \tau_{02}, \tau_{03})$ and plot it in Fig. 3(c). It can be quite perplexing to display this three-dimensional function. Instead, slices with two fixed τ_{03} are plotted to show the property of HG_4. Similarly, in the case of $\tau_{01} = \tau_{02} = \tau_{03}$, corresponding to a body diagonal in Fig. 3(c), the FWHM of the fourth-order correlation function is the broadest. While in the case of $\tau_{01} + \tau_{02} + \tau_{03} = 0$, corresponding to a plain perpendicular to that body diagonal, the FWHM tends to be narrower. Note that under this condition, the relation among τ_{01}, τ_{02}, and τ_{03} is not completely specified. Further analyses show that the greater these variables differ from each other, the narrower the width of HG_4 can be, meanwhile, with a smaller constant term. According to theoretical calculation, the FWHM can shrink to only 30% of the broadest case and the constant background reduces from 4 to 1. The experimentally measured HG_4 is plotted in Fig. 3(d). Less detailed information as it contains, it exhibits consistent property of time sequence. To verify the university of the above law, we further calculate the ninth-order correlation along different time series. Based on our method, the eight-dimensional function $HG_9(\tau_{01}, \tau_{02}, \ldots, \tau_{08})$ can be simplified as a one-dimensional function $HG_9(\tau)$. Experimental results show that the FWHM of $HG_9(-4\tau, -3\tau, -2\tau, -\tau, \tau, 2\tau, 3\tau, 4\tau)$ is only 37% of that of $HG_9(\tau, \tau, \tau, \tau, \tau, \tau, \tau, \tau)$, so the former can definitely yield images with higher resolution. Here, although only a specific time series of the correlation function is taken into consideration, this series makes more contributions to resolution enhancement.

To demonstrate the enhancement of resolution, we explore the ability of our HG method to differentiate unresolved QDs that are separated by a distance shorter than the optical diffraction limit. To avoid the masking of dim emitters in high-order images caused by brightness distortion, we adopt simple linearization using the deconvolution method based on a Lucy–Richardson algorithm [14]. Figure 4(a) displays the mean image and the 2nd-, 4th-, 9th-, 16th-, and 25th-order HG images of a pair of QDs. The relative intensities of them are determined by both their brightness and their specific blinking behavior. So the brighter one in the mean image appears to be a darker one in high-order correlation images. It can be seen that as the correlation order increases, the width of the PSF shrinks remarkably and the unresolved QDs are clearly separate from each other, as shown in HG_{16} and HG_{25} images, which demonstrates significant resolution enhancement. Note that in theory, the PSF of an imaging system can shrink below one pixel size as the order of correlation goes up; in such a manner, imaging resolution is limited by the pixel size in the 25th-order image. It is feasible to get a more accurate measurement of the

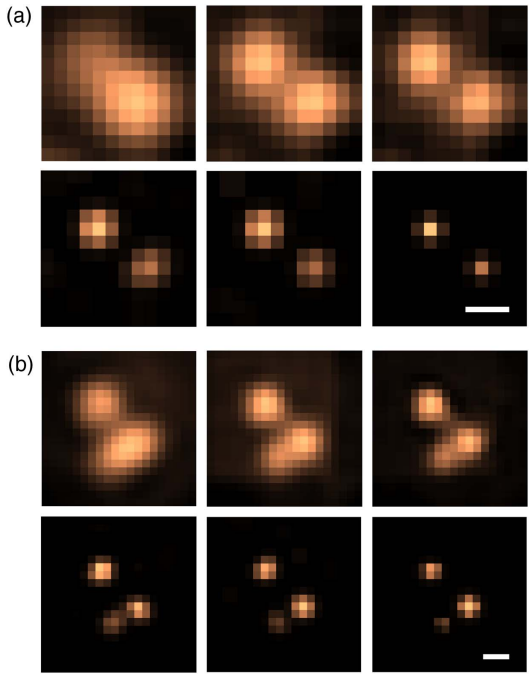

Fig. 4. Experimental high-order correlation images based on the HG method. Data are recorded in series of 1000 frames (100 ms per frame). Resolution enhancement of HG images is shown with (a) a pair of QDs and (b) three close-by QDs. From left to right: mean image and the 2nd-, 4th-, 9th-, 16th-, and 25th-order HG images. Scale bar: 300 nm.

effective PSF by using a camera with a denser pixel array or smaller pixel size. On the other hand, subpixel resolution can be obtained by taking the spatial correlation of different pixels into consideration [17]. Figure 4(b) gives the experimental results of three close-by QDs. As can be seen, the lower right two of them are better resolved in high-order images and the upper left one becomes sharper, which demonstrates that the HG method not only beats the diffraction limit, but also has the potential to image more complex structures like cells or tissues.

The major superiority of the HG method is speed. To verify its efficiency, we compare our HG algorithm HG_n with the conventional SOFI algorithm C_n. Both methods are performed on the same data, i.e., the data used for Fig. 4(b). All the algorithm programs are written by us using MATLAB and run on an ordinary personal computer (Intel Core i5-3210M CPU, 8GB RAM). To reduce background noise, we calculate correlation images for many time lags, from 1 to 9, and afterward sum all of them (see SI text of [13]). The MATLAB codes for the HG algorithm can be found in Code 1, Ref. [25]. The exact computation times required for both methods are given in Table 1, which demonstrates significant speed gain of the HG method under the same correlation orders. Take the order of 6 as an example, it takes about 40 min to calculate C_6 and reconstruct the sixth-order image. While for the HG algorithm, only 0.47 s is needed to generate the sixth-order image, which is definitely less computation demanding and time consuming.

Table 1. Speed Comparison of HG Imaging and SOFI

	Computation Time (s)	
Correlation Order	HG_n	C_n
2	0.2488	0.3264
3	0.2729	1.7558
4	0.3167	18.4967
5	0.3823	232.0493
6	0.4738	2534.8102

On the other hand, the quality of the final image is the key point of an imaging technique. Admittedly, traditional SOFI performs slightly better than our method in terms of resolution. This is understandable because SOFI transforms correlation functions into cumulant functions, which mathematically cancel all low-order correlation terms to ensure high-resolution enhancement. While in the HG method, we reduce the width of correlation functions by calculating them along specific time series, which still contain low-order contributions to some extent. However, considering both the high efficiency and the ability to break the optical diffraction limit, our HG method can be an attractive alternative to existing techniques.

4. APPLICATION: IMAGING THROUGH SCATTERING MEDIA

Finally, we would like to apply our HG imaging method to imaging through scattering media, which is among the biggest challenges in optics and plays an important role in many biomedical and engineering fields [26]. The effect of scattering can be modeled as a random process of optical path, broadening the PSFs of emitters. When light suffers multiple scattering, a large number of scattering events, the degradation of image quality can be so severe that the object may be hidden from view [27]. Over the years, this degradation has been analyzed with different theories: some rely on a measurable amount of unscattered, "ballistic" photons [28], others require initial access the scattering medium [29], the presence of a known object [30], or the projection of a large number of optical patterns [31]. However, the reconstruction of images remains a difficult theoretical and experimental problem [32]. Recently, the second-order correlation of light field has been applied to retrieve an image in scattering media [11]. Here, we demonstrate that HG imaging is a straightforward alternative with potential to retrieve images of scattered objects with highly enhanced resolution.

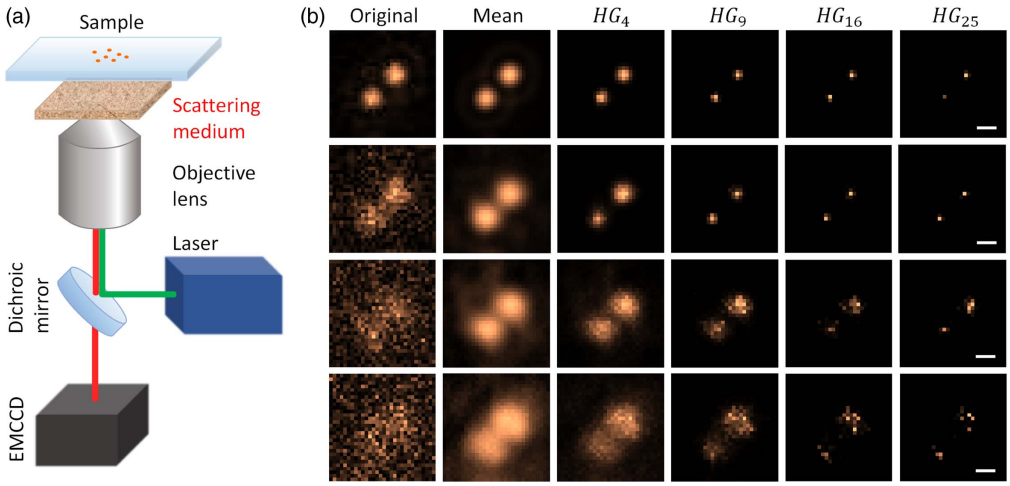

Fig. 5. Experimental HG images of two QDs through scattering media. Data of blinking QDs are recorded in series of 1000 frames (100 ms per frame). (a) Experimental setup of HG imaging system: the scattering medium (rough plastic film) is set between the microscope slide and objective. (b) Experimental results of HG images without (the first row) and with different media that cause increasing scattering (the second, third, and fourth rows). From left to right, each column shows the original image (an arbitrary raw movie frame), mean image (mean intensity of all movie frames), and the 4th-, 9th-, 16th-, and 25th-order of $\mathrm{HG}_n(\tau)$ images, respectively. Scale bar: 500 nm.

The schematic of our experimental setup is shown in Fig. 5(a). We use the same fluorescence microscope and insert different plastic films between the microscope slide and objective as scattering media (single scattering regime). These films are ground by sandpaper with multiple sand sizes, resulting in various degrees of roughness for scattering. Figure 5(b) shows both the comparison of images among different scattering media and among different high orders obtained by using our HG imaging method.

From up to down, the first row shows images of two QDs without scattering media, while the following three rows display results of the same QDs with a rougher and rougher film inserted, corresponding to increasing scattering. As a consequence, the PSF of the system becomes broader and broader, so the quality of the original image degrades distinctly. In the highly scattering case, the signal-to-noise ratio of the raw image is rather low, where the two emitters' scattering patterns fuse into each other and become almost indistinguishable from the background noise. From left to right, the first column shows an arbitrary frame of the raw movie, which is what we directly observed through the EMCCD camera. The second column gives the mean intensity and the following columns are the 4th-, 9th-, 16th-, and 25th-order of $\mathrm{HG}_n(\tau)$ images. We can see that as the order of $\mathrm{HG}_n(\tau)$ goes up, the sizes of two scattered QDs shrink dramatically. As shown in the 16th- and 25th-order images, these QDs can be better resolved, eliminating uncorrelated background noise, even in the highly scattering case. In addition, all high-order images are generated rapidly, getting rid of tedious operation and complicated computation. We expect our method to provide a new insight into the field of optical imaging through scattering media.

5. CONCLUSION

In this study, we have theoretically and experimentally demonstrated an improved imaging method—resolution-enhanced, high-order fluorescence correlation imaging. Compared to the conventional correlation imaging techniques, this method exhibits superior performance for its robustness over a broad range of imaging conditions, including emitters with nonuniform fluctuating behavior and rather low signal-to-noise ratio. By effectively recording and analyzing fluorophores' temporal statistical properties, all individual emitters have been successfully distinguished from background noise. Meanwhile, intractable computation for high-order correlations is reduced by choosing specific time sequences that contribute most to resolution enhancement, which enables efficient high-order imaging. Furthermore, HG imaging has been proved applicable for imaging through scattering media. We have shown that emitters hidden in highly scattering media can be better resolved with significant background reduction and resolution enhancement. Given its simplicity, we anticipate our method will become a complementary and feasible addition to the existing techniques.

APPENDIX A: HG IMAGING PERFORMED ON TUBULIN

To evaluate the imaging capability of our HG method, we also perform a high-order algorithm for a real biological experiment dataset of a tubulin network [33]. The resulting high-order HG images are displayed in Fig. 6. It is clear that as the correlation order increases, the blurred microtubules become sharper, with more unresolved details showing up, which verifies resolution enhancement. On the other hand, as can be seen in Fig. 6(b), the microtubules show discontinuous structures due to nonlinear contrast distortion in high-order reconstruction. The image fidelity can be improved by using the deconvolution method to linearize the contrast response. In addition, note that only 500-frame original pictures are provided in the dataset. If more data are available or the frame rate is higher, better image quality can be achieved based on the statistical analysis of fluctuating samples. Other state-of-the-art SOFI reconstruction algorithms, such as balanced super-resolution optical fluctuation imaging [19] and super-resolution radial fluctuations [34], have also overcome the undesirable image distortion. Given the simplicity and high efficiency of the HG algorithm, we expect that HG imaging can be an alternative method for more applications in biology and other research fields.

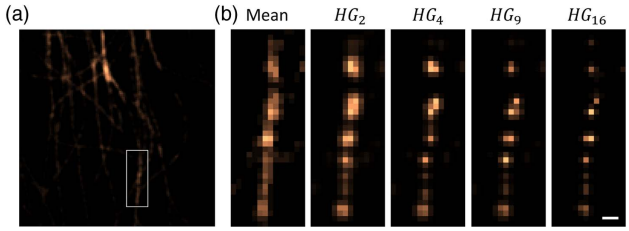

Fig. 6. High-order HG images of real biological experiment dataset. (a) Mean image of the original biological dataset. Data of tubulin are recorded in series of 500 frames (250 ms per frame). Each picture has a size of 128 × 128 pixels (100 nm per pixel). (b) HG images of cropped 40 × 15 pixels marked with the white box in (a). From left to right are the mean image and the 2nd-, 4th-, 9th-, and 16th-order HG images. Fluorescence wavelength: 690 nm. Scale bar: 300 nm.

Funding. National Key Research and Development Program (2016YFA0302500); Shanghai Scientific Innovation Program for International Collaboration (15220721400); Shanghai Scientific Innovation Program (14JC1402900); National Natural Science Foundation of China (NSFC) (11304201, 11674228, 61475100).

REFERENCES

1. E. Abbe, "Beiträge zur Theorie des Mikroskops und der mikroskopischen Wahrnehmung," Archiv für mikroskopische Anatomie **9**, 413–418 (1873).
2. J. Enderlein, "Advanced fluorescence microscopy," Compr. Biomed. Phys. **34**, 111–151 (2014).
3. S. W. Hell and J. Wichmann, "Breaking the diffraction resolution limit by stimulated emission: stimulated-emission-depletion fluorescence microscopy," Opt. Lett. **19**, 780–782 (1994).
4. M. G. Gustafsson, "Nonlinear structured-illumination microscopy: wide-field fluorescence imaging with theoretically unlimited resolution," Proc. Natl. Acad. Sci. U. S. A. **102**, 13081–13086 (2005).
5. S. T. Hess, T. P. Girirajan, and M. D. Mason, "Ultra-high resolution imaging by fluorescence photoactivation localization microscopy," Biophys. J. **91**, 4258–4272 (2006).
6. M. J. Rust, M. Bates, and X. Zhuang, "Sub-diffraction-limit imaging by stochastic optical reconstruction microscopy (STORM)," Nat. Methods **3**, 793–796 (2006).

7. T. B. Pittman, Y. H. Shih, D. V. Strekalov, and A. V. Sergienko, "Optical imaging by means of two-photon quantum entanglement," Phys. Rev. A **52**, R3429(R) (1995).
8. A. Valencia, G. Scarcelli, M. D'Angelo, and Y. Shih, "Two-photon imaging with thermal light," Phys. Rev. Lett. **94**, 063601 (2005).
9. P. Walther, J. W. Pan, M. Aspelmeyer, R. Ursin, S. Gasparoni, and A. Zeilinger, "De Broglie wavelength of a non-local four-photon state," Nature **429**, 158–161 (2004).
10. J. Simon, J. Liu, Y. Shih, and Y. Zhou, "Resolution enhancement of third-order thermal light ghost imaging in the photon counting regime," J. Opt. Soc. Am. B **29**, 377–381 (2012).
11. W. Gong and S. Han, "Correlated imaging in scattering media," Opt. Lett. **36**, 394–396 (2011).
12. W. Gong, P. Zhang, X. Shen, and S. Han, "Imaging in scattering media via the second-order correlation of light field," Opt. Lett. **36**, 394–396 (2009).
13. T. Dertinger, R. Colyer, G. Iyer, S. Weiss, and J. Enderlein, "Fast, background-free, 3D super-resolution optical fluctuation imaging (SOFI)," Proc. Natl. Acad. Sci. U. S. A. **106**, 22287–22292 (2009).
14. M. K. Kim, C. H. Park, C. Rodriguez, Y. K. Park, and Y. H. Cho, "Superresolution imaging with optical fluctuation using speckle patterns illumination," Sci. Rep. **5**, 16525 (2015).
15. T. Dertinger, M. Heilemann, R. Vogel, M. Sauer, and S. Weiss, "Superresolution optical fluctuation imaging with organic dyes," Angew. Chem. **49**, 9441–9443 (2010).
16. O. Schwartz, J. M. Levitt, R. Tenne, S. Itzhakov, Z. Deutsch, and D. Oron, "Superresolution microscopy with quantum emitters," Nano Lett. **13**, 5832–5836 (2013).
17. D. Thomas, C. Ryan, V. Robert, E. Jörg, and W. Shimon, "Achieving increased resolution and more pixels with Superresolution Optical Fluctuation Imaging (SOFI)," Opt. Express **18**, 18875–18885 (2010).
18. S. C. Stein, A. Huss, D. Hähnel, I. Gregor, and J. Enderlein, "Fourier interpolation stochastic optical fluctuation imaging," Opt. Express **23**, 16154–16163 (2015).
19. S. Geissbuehler, N. L. Bocchio, C. Dellagiacoma, C. Berclaz, M. Leutenegger, and T. Lasser, "Mapping molecular statistics with balanced super-resolution optical fluctuation imaging (bSOFI)," Opt. Nanosc. **1**, 4 (2012).
20. P. J. Smith, "A recursive formulation of the old problem of obtaining moments from cumulants and vice versa," Amer. Statist. **49**, 217–218 (1995).
21. G. Scarcelli, J. Oh, Y. Kim, and Y. Cho, "Sub-Rayleigh imaging via speckle illumination," Opt. Lett. **38**, 682–684 (2013).
22. M. Kuno, D. P. Fromm, H. F. Hamann, A. Gallagher, and D. J. Nesbitt, "'On'/'off' fluorescence intermittency of single semiconductor quantum dots," J. Chem. Phys. **115**, 1028–1040 (2001).
23. J. Liu and Y. Shih, "Nth-order coherence of thermal light," Phys. Rev. A **79**, 023819 (2009).
24. Y. Zhou, J. Simon, J. Liu, and Y. Shih, "Third-order correlation function and ghost imaging of chaotic thermal light in the photon counting regime," Phys. Rev. A **81**, 1334–1342 (2010).
25. Y. Liu, L. Chen, W. Liu, X. Liang, and W. Wan, "MATLAB codes for HG imaging," https://figshare.com/s/d655ecc7f303605e6f2e.
26. V. Ntziachristos, "Going deeper than microscopy: the optical imaging frontier in biology," Nat. Methods **7**, 603–614 (2010).
27. A. Ishimaru, *Wave Propagation and Scattering in Random Media* (Academic, 1978).
28. L. Wang, P. Ho, C. Liu, G. Zhang, and R. Alfano, "Ballistic 2-D imaging through scattering walls using an ultrafast optical Kerr gate," Science **253**, 769–771 (1991).
29. O. Katz, E. Small, Y. Bromberg, and Y. Silberberg, "Focusing and compression of ultrashort pulses through scattering media," Nat. Photonics **5**, 372–377 (2011).
30. H. He, J. Zhou, and Y. Guan, "Image restoration through thin turbid layers by correlation with a known object," Opt. Express **21**, 12539–12545 (2013).
31. T. Chaigne, O. Katz, A. C. Boccara, M. Fink, E. Bossy, and S. Gigan, "Controlling light in scattering media non-invasively using the photoacoustic transmission matrix," Nat. Photonics **8**, 58–64 (2013).
32. H. P. Baltes, *Inverse Source Problems in Optics* (Springer-Verlag, 1978).
33. N. Olivier and D. Keller, "LEB, and EPFL," 2018, http://bigwww.epfl.ch/smlm/datasets/index.html?p=../challenge2013/datasets/Real_High_Density.
34. N. Gustafsson, S. Culley, G. Ashdown, D. M. Owen, P. M. Pereira, and R. Henriques, "Fast live-cell conventional fluorophore nanoscopy with ImageJ through super-resolution radial fluctuations," Nat. Commun. **7**, 12471 (2016).